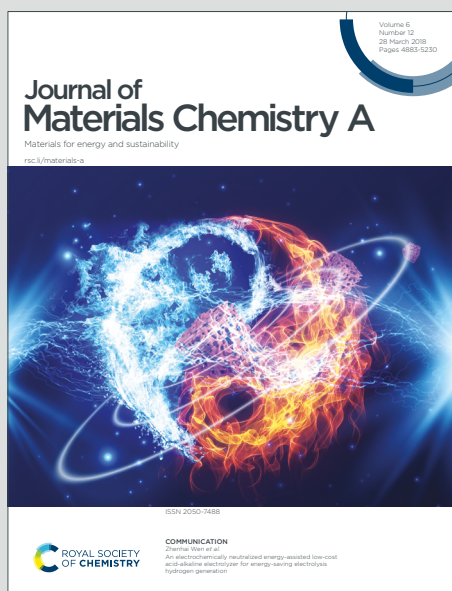


# Journal of Materials Chemistry A

Materials for energy and sustainability

Accepted Manuscript

This article can be cited before page numbers have been issued, to do this please use: A. Plewa, A. Kulka, E. Hanc, W. Zajac, J. Sun, L. Li and J. Molenda, *J. Mater. Chem. A*, 2020, DOI: 10.1039/C9TA11565J.



This is an Accepted Manuscript, which has been through the Royal Society of Chemistry peer review process and has been accepted for publication.

Accepted Manuscripts are published online shortly after acceptance, before technical editing, formatting and proof reading. Using this free service, authors can make their results available to the community, in citable form, before we publish the edited article. We will replace this Accepted Manuscript with the edited and formatted Advance Article as soon as it is available.

You can find more information about Accepted Manuscripts in the [Information for Authors](#).

Please note that technical editing may introduce minor changes to the text and/or graphics, which may alter content. The journal's standard [Terms & Conditions](#) and the [Ethical guidelines](#) still apply. In no event shall the Royal Society of Chemistry be held responsible for any errors or omissions in this Accepted Manuscript or any consequences arising from the use of any information it contains.

# Facile aqueous synthesis of high performance $\text{Na}_2\text{FeM}(\text{SO}_4)_3$ $\text{M}=\text{Fe, Mn, Ni}$ alluaudites for low cost Na-ion batteries

View Article Online  
DOI: 10.1039/C9TA11565J

Anna Plewa<sup>ab</sup>, Andrzej Kulka<sup>a</sup>, Emil Hanc<sup>bc</sup>, Wojciech Zając<sup>a</sup>, Jianguo Sun<sup>b</sup>, Li Lu<sup>bd</sup>, Janina Molenda<sup>a</sup>

<sup>a</sup> AGH University of Science and Technology, Faculty of Energy and Fuels, al. Mickiewicza 30, 30-059 Krakow, Poland

<sup>b</sup> National University of Singapore, Faculty of Mechanical Engineering, Singapore, 117575 Singapore

<sup>c</sup> Mineral and Energy Economy Research Institute, Polish Academy of Sciences, ul. Wybickiego 7, 31-261 Krakow, Poland

<sup>d</sup> National University of Singapore Suzhou Research Institute, Suzhou, 215123, China

## Abstract

A new method of synthesis of stoichiometric  $\text{Na}_2\text{FeM}(\text{SO}_4)_3$  ( $\text{M}=\text{Fe, Mn, Ni}$ ) materials is developed. The proposed unique methodology is based on a facile processing of dissolution of  $\text{Na}_2\text{SO}_4$  and transition metals (Fe, Mn, and Ni) sulfates in an aqueous solution, solvent evaporation, and annealing. This novel method is characterized by a very low degree of complexity but still ensures the highest purity, resulting to high purity of Mn and Ni substituted alluaudite compounds. Synthesized materials possess nanometric size grains with uniform composition distribution.  $\text{Na}_2\text{FeM}(\text{SO}_4)_3$  exhibits great transport properties with low charge transport activation energy related to sodium ions diffusion. Electrochemical characterization of the processed  $\text{Na}_2\text{Fe}_2(\text{SO}_4)_3$  compound in both formats of half-cell and full cell demonstrates the highest power density among all polyanion Na cathodes.

## Keywords

Na-ion batteries; Cathodes; Alluaudite structure;  $\text{Na}_2\text{Fe}_2(\text{SO}_4)_3$ ; Electrochemical properties

## 1. Introduction

View Article Online  
DOI: 10.1039/C9TA11565J

Searching for energy storage technologies in large-scale systems is a challenge for the 21<sup>st</sup> century. Due to the limited availability of raw materials and related severe economic constraints, the use of Li-ion batteries seems to be not the ultimate solution.

To address this issue, many new electron carriers such as sodium, potassium, aluminum, etc. are considered to replace lithium. Of these candidates, Na has already demonstrated a number of advantages for Na-ion batteries such as earth abundant, high value of operating voltage and high electrochemical capacity, and hence high energy density, which is a key parameter for large-scale energy storage <sup>1</sup>. In the search for electrode materials for Na-ion systems, iron-based, cobalt-free polyanionic compounds, including alluaudite sulfates, are now of a great interest <sup>2-4</sup>. Because of the strong covalent bonding in (SO<sub>4</sub>)<sup>n-</sup>, these materials exhibit high structural stability, which makes them especially interesting for commercial applications. The chemical formula of the alluaudite sulfates compounds can be written as AA'BM<sub>2</sub>(SO<sub>4</sub>)<sub>3</sub>, where Na ions are located in three different crystallographic positions: partially occupied A and A' and fully occupied B while M site is filled with Fe <sup>5</sup>. Such arrangement results in a three-dimensional network, characterized by the existence of the open channels along the [001] crystallographic directions in which Na ions may diffuse with low activation energy.

The alluaudite phase has been firstly reported as phosphates, molybdates, and arsenates compounds, and recently, sodium iron sulfates have been also found to crystallize in an alluaudite-type structure <sup>6-9</sup>. Na<sub>2</sub>Fe<sub>2</sub>(SO<sub>4</sub>)<sub>3</sub> phase is a very attractive candidate for battery applications because of its high Fe<sup>3+</sup>/Fe<sup>2+</sup> redox potential (3.8 V vs. Na/Na<sup>+</sup>), particularly large energy density (>450 Whkg<sup>-1</sup> vs. Na/Na<sup>+</sup>), a tunnel-type structure enabling fast ion diffusion and its composition containing only Earth-abundant elements. Recent computational study concerning a stability of the Na<sub>2</sub>Fe<sub>2</sub>(SO<sub>4</sub>)<sub>3</sub> suggested that substitution within the Fe sublattice with other 3d elements to be possible, and an introduction of Ni or Co results in presence of the oxygen anion activity in the redox reactions <sup>10</sup>. Although electrochemical properties of the Na<sub>2+2y</sub>M<sub>2-y</sub>(SO<sub>4</sub>)<sub>3</sub> (M=Fe, Mn, Ni, Co) systems are promising <sup>10-12</sup>, the

synthesis of such  $\text{SO}_4$ -based compounds is demanding due to their tendency towards thermal decomposition and dissolution in water<sup>9,13</sup>. In addition, it is desirable to obtain a compounds  $\text{Na}_{2+2y}\text{M}_{2-y}(\text{SO}_4)_3$  with a Na: M ratio close to 2: 2, in order to fully utilize its electrochemical capacity. However, the synthesis methods adopted so far could only produce materials with large non-stoichiometry (y), e.g.  $\text{Na}_{2.56}\text{Fe}_{1.72}(\text{SO}_4)_3$ ,  $\text{Na}_{2.44}\text{Mn}_{1.79}(\text{SO}_4)_3$  and  $\text{Na}_{2.32}\text{Co}_{1.84}(\text{SO}_4)_3$ <sup>11,14,15</sup> which results in a diminished concentration of 3d metals limiting their specific charge. Most of the previously published works were focused on a synthesis, structural characterization and electrochemical performance of iron-based materials, whereas manganese or nickel compounds, despite they potentially offer higher energy density, were barely examined<sup>10</sup>.

Until now only limited synthesis methods were used to obtain  $\text{Na}_{2+2y}\text{M}_{2-y}(\text{SO}_4)_3$  compounds. Since low-temperature solid-state methods are the most popular,  $\text{Na}_2\text{SO}_4$  and  $\text{FeSO}_4 \cdot 7\text{H}_2\text{O}$  were first proposed as precursors for  $\text{Na}_{2+2y}\text{Fe}_{2-y}(\text{SO}_4)_3$ <sup>9</sup>. In this proposed process,  $\text{Na}_2\text{SO}_4$  and dehydrated  $\text{FeSO}_4$  (obtained by drying  $\text{FeSO}_4 \cdot 7\text{H}_2\text{O}$  under vacuum) are ball-milled in the 3: 2 molar ratio for 6 h then heated twice at 350 °C for 24 h under a continuous Ar gas flow<sup>14</sup>. Another method for obtaining alluaudite compounds is to use ionothermal synthesis based on mixing  $\text{Na}_2\text{SO}_4$  and  $\text{FeSO}_4 \cdot \text{H}_2\text{O}$  (3: 4) with EMI-TFSI ionic liquid using acetone as washing medium in an autoclave at 300 °C<sup>16</sup>. Recently the synthesis in an aqueous medium by using spray drying or Pechini method was proposed<sup>17</sup>. Spray drying was performed using an aqueous solution of commercially available precursors ( $\text{Na}_2\text{SO}_4$  and  $\text{FeSO}_4 \cdot 7\text{H}_2\text{O}$ ) and was carried out in a two-step procedure involving the formation of an intermediate complex in the spray drying chamber followed by annealing (350 °C) for 6 h to form the final product. In the case of the Pechini method also two-step aqueous synthesis was used, by mixing a solution of the same commercially available  $\text{SO}_4$ -precursors with a complexing agent such as  $\text{Na}_2\text{-EDTA} \cdot 2\text{H}_2\text{O}$ , which is the key element. This solution is heated to evaporate water excess and an intermediate product is then annealed at 350 °C for 6 h in argon atmosphere. Both of presented synthesis methods in aqueous medium allow obtaining a non-stoichiometric  $\text{Na}_{2.44}\text{Fe}_{1.78}(\text{SO}_4)_3$  product characterized by a large deviation in Na: Fe ratio, thus severely limiting the  $\text{Na} \mid \text{Na}^+ \mid \text{Na}_{2.44}\text{Fe}_{1.78}(\text{SO}_4)_3$  cell capacity to 70 mAh  $\text{g}^{-1}$ <sup>17</sup>. There are also a few methods for the synthesis of  $\text{Na}_{2+2y}\text{Fe}_{2-y}(\text{SO}_4)_3$  using carbon additives, such

as single wall nanotubes<sup>18</sup>, Ketjen<sup>19</sup>, graphene oxide<sup>20</sup> or reduced graphene oxide<sup>21,22</sup>, which require additional preparation.

Previously reported processing methods are characterized by a high degree of complexity, require a long time of synthesis and high input of energy. Moreover, additional efforts need to be made to protect the highly reactive anhydrous  $\text{FeSO}_4$  against rehydration and to provide a protective atmosphere during the entire synthesis process to prevent the oxidation of  $\text{Fe}^{2+}$ . Besides that, the methods available up to now are not effective because of formation of a large content of impurities, up to 16 wt.% of  $\text{FeSO}_4$  or  $\text{Na}_6\text{Fe}(\text{SO}_4)_4$ , or non-stoichiometric  $\text{Na}_{2+2y}\text{M}_{2-y}(\text{SO}_4)_3$  materials. Among all techniques, spray drying or Pechini method give products with the largest non-stoichiometry and the worst electrochemical performances.

In this paper, we present a new method of synthesis of sulfate cathode materials for alluaudite-structured cathode and Na-ion batteries. After analyzing the difficulties and shortcomings of previously described methods, we developed an easy and cost-effective processing method to synthesize stoichiometric  $\text{Na}_2\text{FeM}(\text{SO}_4)_3$  ( $\text{M}=\text{Fe}, \text{Mn}, \text{Ni}$ ) compounds. This new method can avoid the formation of impurities by a simple addition of excess sodium hence obtain high-quality cathodes. In order to fully take advantage of the proposed procedure, we adopted a comprehensive approach allowing a step-by-step monitoring of the synthesis process using *in-situ* high temperature XRD, thermogravimetric measurement with mass spectrometry, ICP, and XPS techniques. Nanomaterials  $\text{Na}_2\text{FeM}(\text{SO}_4)_3$  synthesized according to our procedure are successfully used as cathodes in Na-ion full cells. A prototype of Na-ion full cell consisting of  $\text{Na}_2\text{FeM}(\text{SO}_4)_3$  cathode synthesized in this work and commercial  $\text{TiO}_2$  as the anode without presodiation is finally successfully developed, which demonstrates a new perspective for development of nontoxic and low cost batteries.

## 2. Experimental section

The reported procedure of synthesis in an aqueous medium is based on our recently patented method<sup>23</sup>. All investigated materials ( $\text{Na}_2\text{Fe}_2(\text{SO}_4)_3$ ,  $\text{Na}_2\text{FeMn}(\text{SO}_4)_3$  and  $\text{Na}_2\text{FeNi}(\text{SO}_4)_3$ ) were prepared using the following process. Raw materials:  $\text{FeSO}_4 \cdot 7\text{H}_2\text{O}$  (Sigma-Aldrich,  $\geq 99\%$ ),  $\text{Na}_2\text{SO}_4$

(Sigma-Aldrich,  $\geq 99.99\%$ ),  $\text{MnSO}_4 \cdot \text{H}_2\text{O}$  (Sigma-Aldrich,  $\geq 99\%$ ) or  $\text{NiSO}_4 \cdot 6\text{H}_2\text{O}$  (Sigma-Aldrich,  $\geq 98\%$ ) were used as obtained from the supplier, without further purification. All the sulfates were dissolved in distilled water and mixed in a stoichiometric ratio. For selected samples, the effect of excess sodium and presence of glucose (D-(+)-glucose, Sigma-Aldrich,  $\geq 99.5\%$ ) was investigated. Excess sodium was introduced in a form of  $\text{CH}_3\text{COONa}$  (Sigma-Aldrich,  $\geq 99\%$ ). Then the solution was heated at  $130^\circ\text{C}$  during continuous mixing, until complete evaporation of water. Such obtained dry precursor was pelletized and annealed at  $350^\circ\text{C}$  for 12 h in a reducing atmosphere (5 vol.%  $\text{H}_2$  in Ar).

The crystal structure of the obtained materials was investigated by X-ray diffraction method using PANalytical Empyrean diffractometer with  $\text{CuK}\alpha$  radiation. The *in-situ* high temperature XRD studies were performed using an Anton Paar HTK 1200N high temperature oven chamber. Phase analysis was based on the matching pattern with PDF4+ (2016) database records. The parameters of the crystal structure and phase contents were refined using the Rietveld method with the GSAS/EXPGUI software package<sup>24,25</sup>. Chemical composition analysis was performed by inductively coupled plasma atomic emission spectroscopy method (ICP-AES) using PerkinElmer Optima 5300V spectrometer. The morphology of all samples was characterized by means of scanning electron microscopy (SEM), using Shimadzu S-4300 scanning electron microscope. Additionally, the measurement of the particle size was provided using the Mastersizer 3000 laser diffraction analyzer. BET surface areas were measured using Micromeritics Instrument Corp. Gemini 2380 specific surface area analyzer. To better understand reactions occurring during the synthesis of the materials as well as to evaluate stability of the product, thermal-gravimetric analysis coupled with mass spectrometry (TG-MS) was carried out. Mass changes were recorded using TA Q5000 IR thermobalance. 30– 50 mg of the powder was placed onto a Pt sample crucible and heated from  $25^\circ\text{C}$  to  $500^\circ\text{C}$  with a heating rate of  $5^\circ\text{min}^{-1}$  in an argon-hydrogen 5% gas with flow rate of  $100\text{ cm}^3\text{ min}^{-1}$ . The Pfeiffer Vacuum ThermoStar mass spectrometer was used to identify the composition of the evolved gases during heating. XPS measurement was performed using a Kratos AXIS UltraDLD spectrometer applying a monochromatic Al K $\alpha$  X-ray source (1486.71 eV photons) and a dwelling time of 100 ms. The binding energy of the spectra was calibrated against C 1s peak at 285 eV. The XPS spectra were mathematically fitted using XPSPEAK41 software. Electrical

conductivity in air atmosphere was measured in the 25 °C– 360 °C temperature range during heating, with 20 °C steps, by means of impedance spectroscopy method using Solartron Analytical SI 1260 impedance/gain-phase analyzer with sinusoidal excitation voltage equal 0.1 V. To ensure good electrical contact between the sample and the electrodes, Au was sputtered on both sides of a polished disk sample. The resistance values were calculated by fitting the equivalent circuit parameters to the impedance spectra in Zview 3.5d Scribner Associates software.

Electrochemical studies were carried out in Na | Na<sup>+</sup> | Na<sub>2</sub>FeM(SO<sub>4</sub>)<sub>3</sub> and TiO<sub>2</sub> | Na<sup>+</sup> | Na<sub>2</sub>FeM(SO<sub>4</sub>)<sub>3</sub> cells. The 1M solution of NaPF<sub>6</sub> (Sigma-Aldrich, 99.99%) in 1: 1 mixture of ethylene carbonate (EC, Sigma-Aldrich, 99.99%) and diethyl carbonate (DEC, Sigma-Aldrich, 99.99%) were used as electrolytes. Sodium metal (Sigma-Aldrich, 99.9%) was used as a negative electrode for half cells. Whereas, commercial TiO<sub>2</sub> (Sigma-Aldrich, anatase, nanopowder, 99.7%) as an active material mixed with polyvinylidene difluoride (PVDF) binder (10 wt.%) and carbon black (10 wt.%) was used as an anode in full cells. For the positive electrode, the active material Na<sub>2</sub>FeM(SO<sub>4</sub>)<sub>3</sub> (80 wt.%) was mixed with polyvinylidene difluoride (PVDF) binder (10 wt.%) and carbon black (10 wt.%). For the preparation of the slurries of anode and cathode N-methyl-2-pyrrolidone (NMP) was added, in order to obtain the proper viscosity. The prepared slurries were coated on Al foil for cathode and anode, then dried at 80 °C. Both electrodes, cut in a form of 12-mm-diameter discs, were pressed and dried again at 120 °C for 12 h in a vacuum, the loading of the active electrodes materials was in the range of 1- 3 mg per cm<sup>2</sup>. Glass microfiber filter (Whatman, GF/A) was used as a separator. Coin-type CR2016 electrochemical cells were assembled in a glove box (UNILAB, M. Braun) under an argon atmosphere, with controlled oxygen and water vapor pressure (<0.1 ppm). Charge/discharge curves were recorded from 2 to 4.5 V at C/10 current rates using both MACCOR and LAND battery cycler galvanostat. Rate capability was measured at different current rate of 10 μA (C/20), 15 μA, 20 μA, 25 μA. Cyclic voltammetry study was carried out using an Autolab PGSTAT302 with a scanning rate of 0.05 mV s<sup>-1</sup> from 2 to 4.5 V. The internal impedance of the half cells was measured by an AC impedance method using SI 1260 impedance/gain-phase analyzer (Solartron Analytical). Data were collected in the range of 0.01Hz–100 kHz.



### 3. Results and discussion

View Article Online  
DOI: 10.1039/C9TA11565J

#### 3.1. Synthesis procedure and phase composition

In the initial trials, stoichiometric amounts of  $\text{Na}_2\text{SO}_4$  and  $\text{FeSO}_4$  precursor were used. The XRD studies of the as-synthesized compounds revealed existence of multiphase mixture composed of 76 wt.%  $\text{Na}_2\text{Fe}_2(\text{SO}_4)_3$  and 24 wt.%  $\text{FeSO}_4$  (Fig. 1), which is in line with other reported observations due to sodium deficiency in product when stoichiometric amounts of precursors were used<sup>9,14</sup>. Therefore, in order to eliminate iron sulfate impurities formation, excess of sodium was used. For this purpose,  $\text{CH}_3\text{COONa}$  as a Na reservoir was chosen (0–30 mol.% in relation to the amount of Na), due to its good solubility in water. We noted that difficulty in obtaining high purity  $\text{Na}_2\text{Fe}_2(\text{SO}_4)_3$  is also associated with easy iron oxidation,  $\text{Fe}^{2+} \rightarrow \text{Fe}^{3+}$  during synthesis. Therefore to prevent iron ions from oxidation and preserve the reducing environment, glucose additive was used (15 wt.% in relation to the assumed amount of the product). Furthermore, glucose additive also acts as an additional carbon precursor, which after pyrolysis forms an evenly distributed film on the active material grains improving electrical contact and reducing the electrode overpotential.

The detailed structural analysis was conducted for the samples synthesized with different sodium excess and glucose concentration in order to examine the presence of C2/c alluaudite structure and quantify the content of impurity phases. XRD patterns for the samples with different amount of glucose and  $\text{CH}_3\text{COONa}$  are shown in Fig. 1a, where materials are divided into two groups. The first group contains materials without glucose while the second one includes samples with a constant amount of glucose additive (15 wt.%). Concentration of  $\text{CH}_3\text{COONa}$  in both groups was 0, 20, 25 and 30 mol.%. The Rietveld analysis for all obtained diffractograms allowed us to draw the phase composition diagram of the final product depending on glucose and  $\text{CH}_3\text{COONa}$  contents (Fig. 1b). The material obtained without additives is characterized by the proportion between  $\text{Na}_2\text{Fe}_2(\text{SO}_4)_3$  and iron sulfate ratio equal to 76: 24 by weight. When 20 mol.% addition of  $\text{CH}_3\text{COONa}$  is used, an increase of the amount of  $\text{Na}_2\text{Fe}_2(\text{SO}_4)_3$  phase up to 87 wt.% is noted. When 25 mol.%  $\text{CH}_3\text{COONa}$  was used, purity of the alluaudite phase increased to 92 wt.%, with as little as 8 wt.% of  $\text{FeSO}_4$ . Similar relation was observed for glucose additive series, while in this case the purity was even higher. When 25 mol.% of  $\text{CH}_3\text{COONa}$



together with 15 wt.% of glucose was used, the amount of  $\text{Na}_2\text{Fe}_2(\text{SO}_4)_3$  in the final product increased up to 98 wt.% (refinement data are included in Supplementary material Table S1, S2 and Fig. S1). The values of lattice parameters for  $\text{Na}_2\text{Fe}_2(\text{SO}_4)_3/\text{C}$  are higher than presented before:  $a = 11.56 \text{ \AA}$ ,  $b = 12.65 \text{ \AA}$ ,  $c = 6.52 \text{ \AA}$ ,  $\beta = 95^\circ$  and  $V = 947.35 \text{ \AA}^3$ <sup>20</sup>. Moreover, it is noted that if the sodium acetate concentration is higher than 25 mol.%, the  $\text{FeSO}_4$  content increases up to 20 wt.% for both materials with and without glucose. Since the addition of  $\text{CH}_3\text{COONa}$  changes pH of the solution, it is reasonable to deduce that with a decrease in the pH value of the solution, the  $\text{FeSO}_4$  phase could be stabilized.

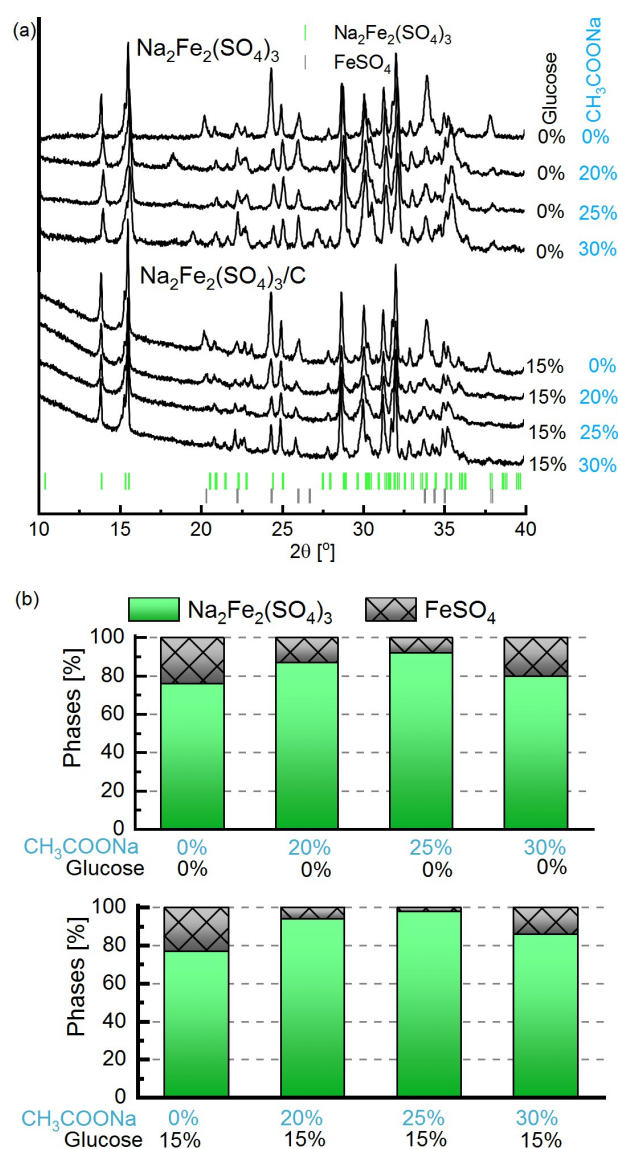


**Fig. 1.** (a) X-ray diffraction patterns for  $\text{Na}_2\text{Fe}_2(\text{SO}_4)_3$  and  $\text{Na}_2\text{Fe}_2(\text{SO}_4)_3/\text{C}$  samples synthesized with different amounts of  $\text{CH}_3\text{COONa}$  and glucose additives and (b) phase composition deduced from these patterns.

Since iron ions should possess 2+ valence in  $\text{Na}_2\text{Fe}_2(\text{SO}_4)_3$ , to confirm the oxidation state XPS measurements were performed. The obtained XPS spectrum for  $\text{Na}_2\text{Fe}_2(\text{SO}_4)_3$ , synthesized with 15 wt.% glucose and 25 mol.%  $\text{CH}_3\text{COONa}$  in the range of Fe 2p electron binding energy is presented in Fig. 2.

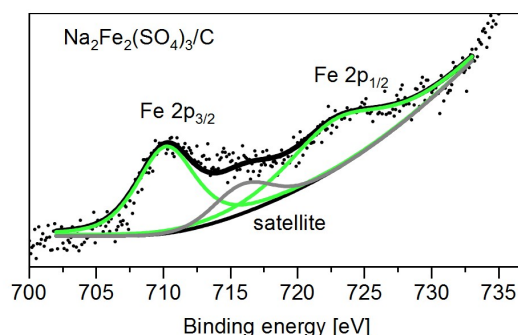


**Fig. 2.** XPS spectrum for  $\text{Na}_2\text{Fe}_2(\text{SO}_4)_3/\text{C}$  sample (15 wt.% glucose, 25 mol.%  $\text{CH}_3\text{COONa}$ ).

Two maxima at about 710 and 723 eV were attributed to the Fe  $2p_{3/2}$  and  $2p_{1/2}$  binding energies respectively. It corresponds well with the other literature reports regarding Fe species in this kind of compounds<sup>26</sup>. These peaks were assigned to the  $\text{Fe}^{2+}$  spectrum, a similar value of binding energy for  $\text{Fe}^{2+}$  is observed in the case of  $\text{FeSO}_4$  or  $\text{Fe}_2(\text{MoO}_4)_3$ <sup>27,28</sup>. Moreover,  $\text{Fe}^{2+}$   $2p_{3/2}$  peak exhibited an asymmetric tail to higher binding energy. This tail was ascribed to surface structures that exhibit different binding energies compared with that of the bulk structure because of surface termination. In this case, the effect of the surface is strong because obtained sample consists of nanograins according to SEM and BET measurements (Fig. 7), which causes strong asymmetry in  $2p_{3/2}$  peak. Furthermore, the presence of satellite peak structures has been observed. Such satellites have been ascribed to shake-up processes. For  $\text{Na}_2\text{Fe}_2(\text{SO}_4)_3$  energy separation between the  $2p_{3/2}$  main peak and the  $2p_{3/2}$  shake-up satellite peak is 5.4 eV, which is similar to that in  $\text{FeSO}_4$ <sup>28</sup>. Based on this data it can be concluded that  $\text{Na}_2\text{Fe}_2(\text{SO}_4)_3$  phase contains only divalence  $\text{Fe}^{2+}$  since the peak from  $\text{Fe}^{3+}$  (about 720 eV<sup>20</sup>) was not observed.

Compared with previous investigations<sup>14,16</sup> reporting instability of stoichiometric  $\text{Na}_2\text{Fe}_2(\text{SO}_4)_3$  phase synthesized using the low temperature nonaqueous method and appearance of  $\text{Fe}^{2+}$  and  $\text{Fe}^{3+}$  ions, the present study using an aqueous solution demonstrates the possibility of synthesis of high purity

$\text{Na}_2\text{Fe}_2(\text{SO}_4)_3$  with minimized amount of  $\text{Fe}^{3+}$  ions. Although two-step synthesis could result in stoichiometric  $\text{Na}_2\text{Fe}_2(\text{SO}_4)_3$ , valence analysis of ion ions still showed mixed divalent and trivalent even protective Ar gas was used in the synthesis. This effect was probably related to iron oxidation during sample loading and testing<sup>20</sup> or presence of impurities with  $\text{Fe}^{+3}$ <sup>9,14</sup>. Since  $\text{Fe}^{3+}$  is non-active, the capacity of the Na-ion cells with mixed divalent and trivalent iron ions shows poor capacity.

In order to confirm stoichiometry of the material obtained from the optimized amount of additives (15 wt.% glucose, 25 mol.%  $\text{CH}_3\text{COONa}$ ) ICP-AES measurement was conducted. The data from the measurement showed that the weight fraction of Na and Fe was 11.1% and 26.8% respectively, implying the molar ratio to be 1:1.

Based on combined XRD, XPS and ICP results, it can therefore be concluded that the stoichiometry of the alluaudite phase had been achieved. Estimated stoichiometry from XRD equal  $\text{Na}_{2.06}\text{Fe}_{1.97}(\text{SO}_4)_3$ . Taking into account that XRD analysis revealed 2 wt.% of  $\text{FeSO}_4$  impurity, XPS clearly confirmed that all iron ions are in the divalence state, whereas according to ICP the Na:Fe atomic ratio was 1:1, we can calculate the stoichiometry  $\text{Na}_{2.04}\text{Fe}_{1.98}(\text{SO}_4)_3$ . This result is very close to  $\text{Na}_2\text{Fe}_2(\text{SO}_4)_3$ . For simplicity, we denote it as  $\text{Na}_2\text{Fe}_2(\text{SO}_4)_3$ .

Until now it is still not clear what roles and mechanisms of additional sodium acetate that assisted formation of single-phase nearly stoichiometric  $\text{Na}_2\text{Fe}_2(\text{SO}_4)_3$  alluaudite. To address this issue, we carried out thermogravimetric measurement with mass spectrometry analysis of the sample  $\text{Na}_2\text{Fe}_2(\text{SO}_4)_3/\text{C}$  (15 wt.% glucose and 25 mol.%  $\text{CH}_3\text{COONa}$ ) during synthesis in argon-hydrogen 5% atmosphere (Fig. 3). First and second mass loss observed around 120 °C and above 200 °C are related to desorption of physically adsorbed water from surface and the release of chemically bound water respectively, which corresponds to ionic current peaks at  $m/z=17$  and 18 related to evolution of  $\text{H}_2\text{O}$ . Above 400 °C a decrease in the mass was noted simultaneously with MS peaks at  $m/z=48$ , 40, 32 and 64 indicating the formation of sulfur oxides  $\text{SO}_x$ . The first increase of ionic current from  $m/z=23$  (Na) and  $m/z=62$  ( $\text{Na}_2\text{O}$ ) is detected above 150 °C, then signal level remains constant indicating continuous evolution of sodium, until second increase is detected above 380 °C pointing to more extensive evolution of sodium, however, determination of exact chemical nature of the evolved sodium containing

chemical species requires further investigations. However, determination of exact chemical nature of the evolved sodium containing chemical species requires further investigations. Total mass loss in this experiment which could be ascribed to evolution of sodium-containing compounds is rather small. However, taking into account that in the whole synthesis period, the sample was annealed for at 350 °C 24h, and since very close to 380 °C, there is a possibility of more significant sodium evaporation. We believe that could be the mechanism explaining why according to ICP analysis results in Na:Fe molar ratio equal to 1, despite the fact sodium in the precursor was excess.

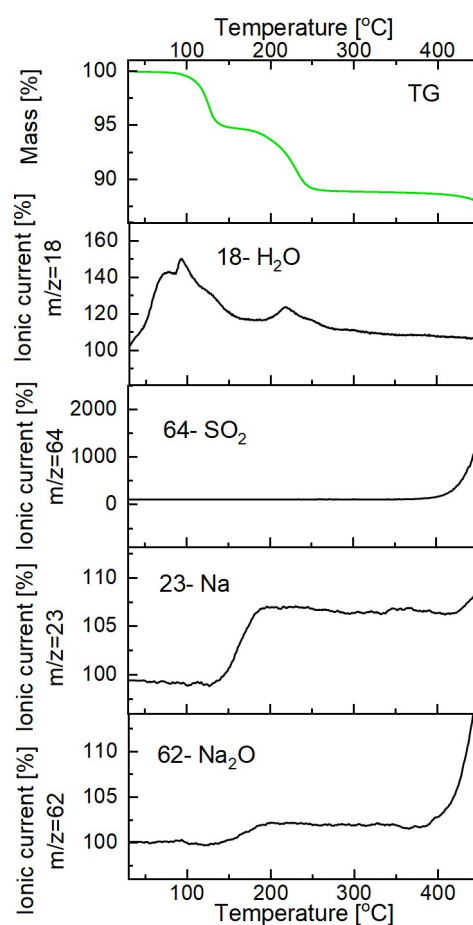


**Fig. 3.** Thermogravimetric measurement of precursor during synthesis correlated with mass spectrometry.

To further understand the mechanisms of  $\text{Na}_2\text{Fe}_2(\text{SO}_4)_3$  formation, *in-situ* high temperature XRD and thermogravimetric measurements were carried out (Fig. 4). Rietveld analysis allowed us to

investigate products of the reactions and phase fraction changes during the synthesis process.  $\text{Na}_2\text{SO}_4$ ,  $\text{FeSO}_4$ , glucose (15 wt.%) and  $\text{CH}_3\text{COONa}$  (25 mol.%) were dissolved in deionized water and dried at 130 °C for 2 h. After water evaporation, the material was used for *in-situ* high temperature XRD measurement with an Ar flow.

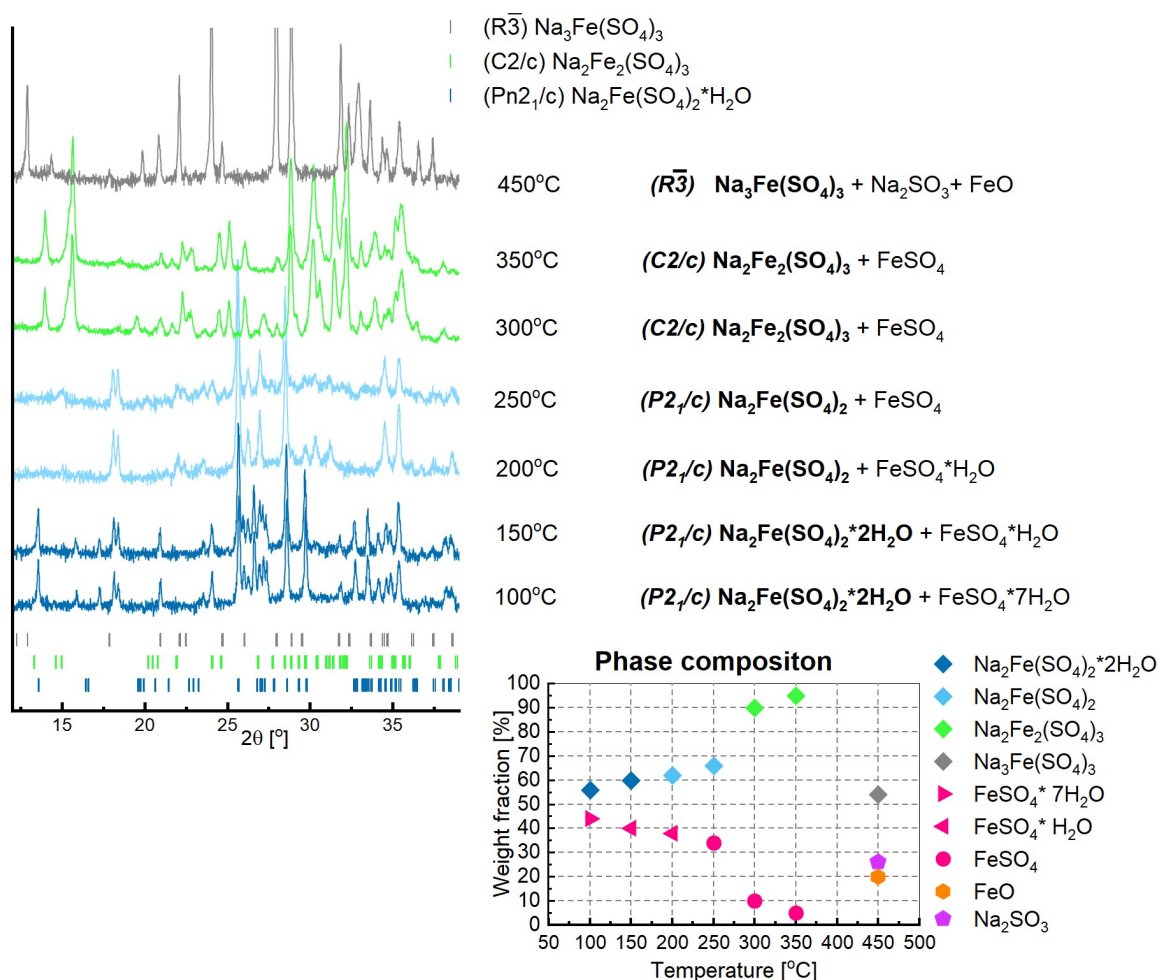


**Fig. 4.** *In-situ* high temperature XRD studies of the formation of the crystalline phases during annealing of the precursor and thermogravimetric analysis of the precursor.

The results showed that after drying at 130 °C for 2 h, two phases, namely  $\text{Na}_2\text{Fe}(\text{SO}_4)_2 \cdot 2\text{H}_2\text{O}$  (monoclinic, P2<sub>1</sub>/c) and  $\text{FeSO}_4 \cdot 7\text{H}_2\text{O}$ , were formed. Evolution of water in steps was observed during heating (evolved gas analysis was based on mass spectrometry investigations presented in Fig. 3). XRD spectra recorded at the same temperature (Fig. 4) showed that the first one, in the range between 100

and 150 °C, was related to water evolution from  $\text{FeSO}_4 \cdot 7\text{H}_2\text{O}$ , whereas the second one in the temperature range from 200 to 250 °C, was ascribed to water evaporation from the  $\text{Na}_2\text{Fe}(\text{SO}_4)_2 \cdot 2\text{H}_2\text{O}$  krönkite-type phase. Crystallization of monoclinic alluaudite phase  $\text{Na}_2\text{Fe}_2(\text{SO}_4)_3$  (space group C2/c) started above 250 °C. At 350 °C alluaudite phase content achieves its maximum of 95 wt.%. Moreover, when the temperature exceeds 400 °C the further mass decline is detected, indicating the formation of the gaseous sulfur dioxide  $\text{SO}_x$ . At 450 °C the structure of the material changes from  $\text{Na}_2\text{Fe}_2(\text{SO}_4)_3$  (C2/c) to  $\text{Na}_3\text{Fe}(\text{SO}_4)_3$  ( $R\bar{3}$ ) with rhombohedral symmetry and impurity phases appear.

Based on the literature, stoichiometric  $\text{Na}_2\text{Fe}_2(\text{SO}_4)_3$  could only be synthesized using two methods: solid-state formation<sup>14</sup> and freeze-drying process<sup>20</sup>, whereas non-stoichiometric materials  $\text{Na}_{2+2y}\text{Fe}_{2-y}(\text{SO}_4)_3$  such as  $\text{Na}_{2.44}\text{Fe}_{1.78}(\text{SO}_4)_3$ <sup>17</sup>,  $\text{Na}_{2.5}\text{Fe}_{1.75}(\text{SO}_4)_3$ <sup>29</sup>,  $\text{Na}_{2.56}\text{Fe}_{1.72}(\text{SO}_4)_3$ <sup>14</sup> could be easily obtained in a variety of various techniques. The complexity of the freeze-drying process is associated with dissolving of sulfate-based substrates in pyrrole and liquid nitrogen under Ar gas atmosphere. Solid-state method leads to obtaining  $\text{Na}_2\text{Fe}_2(\text{SO}_4)_3$  with 17 wt.% of impurities. In both cases, it is necessary to fabricate the anhydrous  $\text{Na}_2\text{SO}_4$  and  $\text{FeSO}_4$  compounds. Compared to them the simplicity of the presented method significantly shortens the synthesis time and reduces the cost of final  $\text{Na}_2\text{Fe}_2(\text{SO}_4)_3$  product.

### 3.2. Determination of carbon content in obtained $\text{Na}_2\text{Fe}_2(\text{SO}_4)_3/\text{C}$ compound

To determine the amount of the residual carbon in the as-synthesized powders, simultaneous TG analysis and mass spectroscopy (MS) analysis was performed (Fig. 5). Two samples, one of which synthesized with 15 wt.% glucose, 25 mol.%  $\text{CH}_3\text{COONa}$  and another one without glucose but only 25 mol.%  $\text{CH}_3\text{COONa}$ , were heated in a flow of synthetic air (Fig. 5a) in order to burn out the carbon and to determine its content from recorded loss of the mass. We noted that it is difficulty to interpret the results arisen from simultaneous oxidation of iron and decomposition of sulfate together with oxidation of carbon. For sample synthesized with sodium acetate but without glucose, TG curve below 500°C revealed increment in weight about 4% , followed by rapid mass drop above 600°C and a plateau above



ca. 700°C at a mass of 86% in relation to the initial value. The weight gain in the first stage can be attributed to oxidation of iron, with a theoretical weight gain of 3.6% based on the oxidation of 2 moles  $\text{Fe}^{2+}$  to  $\text{Fe}^{3+}$  and molar mass of compound. The second stage above 600°C, was attributed to decomposition of sulphate ions by releasing sulfur oxides, as confirmed by a strong MS signal at  $m/z=64$ . Surprisingly, a small MS signal at  $m/z=44$  related to evolution of carbon dioxide with its maximum at ca. 560°C was detected, even though this sample formally did not contain any intentionally added carbon-containing compounds. We assume that it stemmed from decomposition of surface carbonates and does not affect mass of the sample significantly. On the other hand TG curve for the sample synthesized with glucose (15 wt.%) and  $\text{CH}_3\text{COONa}$  (25 mol.%) possessed similar shape. However, two additional small steps of mass loss were noted at 300 and 360°C coupled with intense MS signals at  $m/z=44$  suggesting that they were related to carbon oxidation. Finally, residual mass measured above 700°C for this sample was 83.3%.

Assuming that all other processes were not affected by glucose and sodium acetate, the difference between these two TG curves can be used to calculate the carbon content in the sample synthesized with the additives. The same measurements were taken for samples with Mn and Ni. The calculated value gives the residual carbon content estimated as  $2.7 \pm 0.3$  wt.%. Since the carbon could not be detected by X-ray diffraction, its amorphous state is assumed. Moreover, XPS result (Supplementary material Fig. S2) showed that the studied composite cathode material carbon (C-C) is observed.



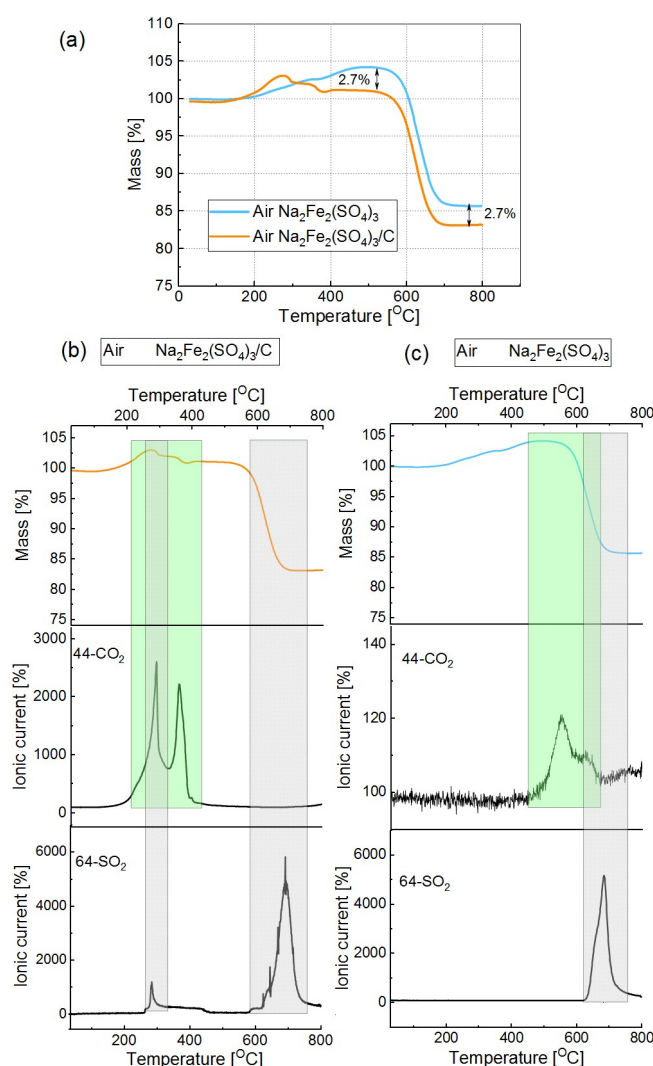


**Fig. 5.** (a) Thermal analysis of  $\text{Na}_2\text{Fe}_2(\text{SO}_4)_2$  and  $\text{Na}_2\text{Fe}_2(\text{SO}_4)_2/\text{C}$  in air flow correlated with mass spectrometry for (b)  $\text{Na}_2\text{Fe}_2(\text{SO}_4)_2/\text{C}$  and (c)  $\text{Na}_2\text{Fe}_2(\text{SO}_4)_2$ .

### 3.3. Iron substitution in $\text{Na}_2\text{FeM}(\text{SO}_4)_3/\text{C}$

Based on the above-described optimized procedure of synthesis of high purity  $\text{Na}_2\text{Fe}_2(\text{SO}_4)_3/\text{C}$  samples, as well as other two less known systems of  $\text{Na}_2\text{FeM}(\text{SO}_4)_3/\text{C}$  ( $\text{M}=\text{Mn}, \text{Ni}$ ) were studied. Fig. 6a presents a Rietveld analysis of powder XRD data for  $\text{Na}_2\text{Fe}_2(\text{SO}_4)_3/\text{C}$ ,  $\text{Na}_2\text{FeMn}(\text{SO}_4)_3/\text{C}$  and  $\text{Na}_2\text{FeNi}(\text{SO}_4)_3/\text{C}$  synthesized with 15 wt.% of glucose and 25mol.% of  $\text{CH}_3\text{COONa}$  at 350 °C. Materials with  $\text{Na}_2\text{FeMn}(\text{SO}_4)_3/\text{C}$  and  $\text{Na}_2\text{FeNi}(\text{SO}_4)_3/\text{C}$  compositions were synthesized with a purity of min. 96%, which is comparable with described above purity of  $\text{Na}_2\text{Fe}_2(\text{SO}_4)_3/\text{C}$  sample, which

demonstrates the capability of the proposed synthesis method to fabricate a wide range of various chemical compositions of the alluaudite sulfates. The refined values of the lattice parameters for a series of  $\text{Na}_2\text{FeM}(\text{SO}_4)_3/\text{C}$  ( $\text{M} = \text{Mn, Fe, Ni}$ ) are presented in Fig. 6b, the value of  $\beta$  is  $115^\circ$  for all compositions. The unit cell volumes are  $964.8 \text{ \AA}^3$ ,  $962.3 \text{ \AA}^3$  and  $957.8 \text{ \AA}^3$  for  $\text{M} = \text{Mn, Fe}$  and  $\text{Ni}$  respectively. As can be seen, the unit cell parameters  $a$ ,  $b$  and  $c$ , and unit cell volume  $V$  change monotonically with ionic radius of 3d metal substitution of Fe by Mn and Ni. The observed relation can be understood taking into consideration ionic radius of  $\text{Mn}^{2+}$  ( $0.83 \text{ \AA}$ ),  $\text{Fe}^{2+}$  ( $0.78 \text{ \AA}$ ),  $\text{Ni}^{2+}$  ( $0.69 \text{ \AA}$ )<sup>30</sup> and indicates formation of solid solution in the  $\text{Na}_2\text{FeM}(\text{SO}_4)_3/\text{C}$  system in the investigated substitution range.

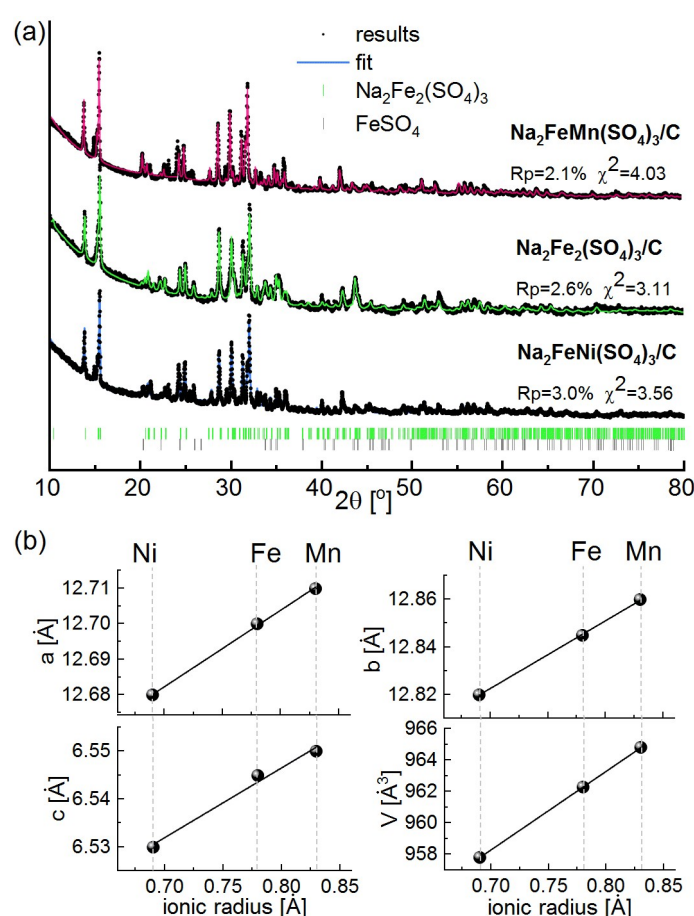


**Fig. 6.** (a) X-Ray diffraction patterns for series of  $\text{Na}_2\text{FeM}(\text{SO}_4)_3$   $\text{M} = \text{Mn, Fe, Ni}$  and (b) evolution of the unit cell volume  $V$ ,  $a$ ,  $b$  and  $c$  parameters as a function of ionic radius.

3.4. Microstructural analysis of  $\text{Na}_2\text{FeMn}(\text{SO}_4)_3/\text{C}$  composites

View Article Online  
DOI: 10.1039/C9TA11565J

Fig. 7a presents exemplary SEM micrographs of  $\text{Na}_2\text{FeMn}(\text{SO}_4)_3/\text{C}$  with EDS analysis of the examined sample. Additionally, SEM micrographs of  $\text{Na}_2\text{Fe}_2(\text{SO}_4)_3/\text{C}$  and  $\text{Na}_2\text{FeNi}(\text{SO}_4)_3/\text{C}$  are presented in Supplementary material (Fig. S3-S5). Fig. 7b and Fig. 7c illustrate grain size distribution measured by laser scattering and BET methods for all the samples.

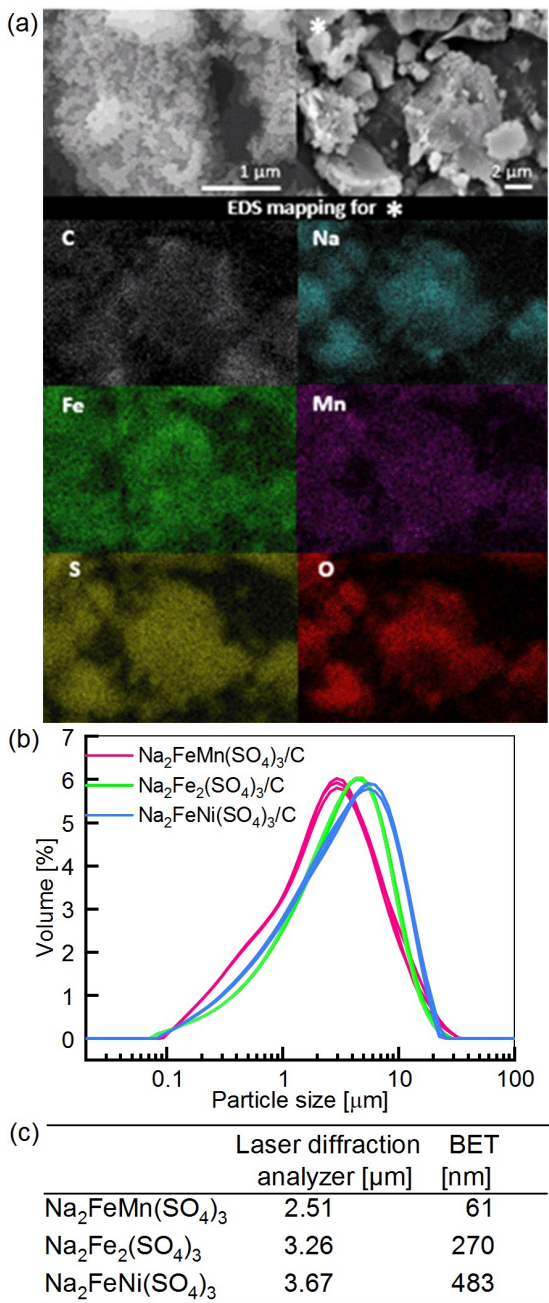


**Fig. 7.** (a) SEM images of  $\text{Na}_2\text{FeMn}(\text{SO}_4)_3$  with EDS analyzing. Results of grain size analyzing with (b) grain size distribution graph and (c) comparison value for two methods.

The particle size ranges from 1 to 10  $\mu\text{m}$  comprised of primary particles about 50-100 nm. View Article Online  
DOI: 10.1039/C9TA11565J

There is no significant change in morphology related to the Fe substitution. Energy dispersive spectroscopy (EDS) analysis of alluaudite Na-Fe-Mn sample was examined to confirm the presence and the location of carbon obtained after glucose pyrolysis. As can be clearly seen, carbon is distributed uniformly in the whole volume of material. Furthermore, the EDS analysis with element mapping for Na, Fe, Mn and S atoms led to the confirmation of a uniform distribution of all constituent elements. In addition, particle size distribution was measured (Fig. 7b). In the obtained  $\text{Na}_2\text{FeM}(\text{SO}_4)_3$  samples micrometric grains were observed, corresponding to the secondary particles detected by the SEM analysis. The size of the particles varies from 2.5  $\mu\text{m}$  for  $\text{Na}_2\text{FeMn}(\text{SO}_4)_3$  to 3.7  $\mu\text{m}$  for  $\text{Na}_2\text{FeNi}(\text{SO}_4)_3$ . Particle size was also calculated from the value of the surface area measured by Brunauer, Emmett, and Teller (BET) technique. The results are 61 nm, 270 nm and 483 nm for  $\text{Na}_2\text{FeMn}(\text{SO}_4)_3$ ,  $\text{Na}_2\text{Fe}_2(\text{SO}_4)_3$  and  $\text{Na}_2\text{FeNi}(\text{SO}_4)_3$  respectively. Similar values of particle size were measured for  $\text{Na}_{2.85}\text{Fe}_{1.57}(\text{SO}_4)_3$  equal 200- 300 nm<sup>22</sup>, 250 nm for  $\text{Na}_2\text{Fe}_2(\text{SO}_4)_3$ <sup>9</sup> and 50- 100 nm for  $\text{Na}_{2.44}\text{Mn}_{1.79}(\text{SO}_4)_3$ <sup>15</sup>. This nanoscale morphology and nanometric grains can be rooted in the low-temperature annealing (350 °C) involving less aggressive grain-growth and developing smaller particles.

### 3.5. Electrical conductivity of $\text{Na}_2\text{FeM}(\text{SO}_4)_3/\text{C}$ composites

Total electrical conductivity of the  $\text{Na}_2\text{FeM}(\text{SO}_4)_3/\text{C}$  composites was measured using impedance spectroscopy technique on disk shaped pellets with gold electrodes sputtered on the opposite surfaces. In order to evaluate the contribution of carbon as well as the alluaudite phase on electrical properties of the composites, bare  $\text{Na}_2\text{Fe}_2(\text{SO}_4)_3$  sample without glucose was used as a reference. The Nyquist plots for  $\text{Na}_2\text{Fe}_2(\text{SO}_4)_3$  and  $\text{Na}_2\text{Fe}_2(\text{SO}_4)_3/\text{C}$  composite measured at 25°C is depicted in Fig. S6. Characteristic low frequency tail for  $\text{Na}_2\text{Fe}_2(\text{SO}_4)_3$  sample indicates dominating ionic conductivity, in agreement with previous reports<sup>31</sup>. Some scattering observed in the tail was probably due to high resistance of the sample. Ionic conductivity of the carbon free sample at 25°C was  $2.5 \cdot 10^{-8} \text{ S cm}^{-1}$ , which is slightly lower than  $1 \cdot 10^{-7} \text{ S cm}^{-1}$  reported for  $\text{Na}_{2.56}\text{Fe}_{1.72}(\text{SO}_4)_3$  by Lu and Yamada<sup>31</sup>. We suppose this discrepancy can be explained by differences in porosity due to different compressing methods and

nonstoichiometry leading to altered concentration of point defects. Contrarily, for the  $\text{Na}_2\text{Fe}_2(\text{SO}_4)_3/\text{C}$  composite sample, the impedance spectrum consisted of a single arc without a low frequency tail suggesting significant contribution of electronic-type conductivity. Total electrical conductivity of the composite sample was approximately two orders of magnitude higher than that of the carbon free sample and reached  $1.4 \cdot 10^{-6} \text{ S cm}^{-1}$  at  $25^\circ\text{C}$ . we assume that the different character and higher values of electrical conductivity are due to the presence of carbon film formed from decomposition of glucose. Despite very low amount of carbon of about 2.7 wt.%, it was still able to reduce the electrical resistance of the composite sample. The obtained values of electrical conductivity as a function of temperature presented as an Arrhenius plot for both carbon free  $\text{Na}_2\text{Fe}_2(\text{SO}_4)_3$  and  $\text{Na}_2\text{Fe}_2(\text{SO}_4)_3/\text{C}$  composite are gathered in Fig. 8a.

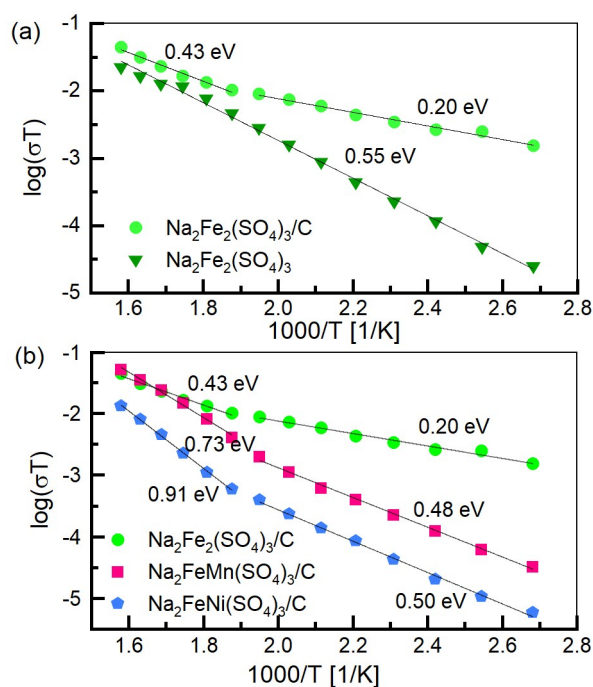


**Fig. 8.** Arrhenius plot of electrical conductivity for (a)  $\text{Na}_2\text{FeM}(\text{SO}_4)_3$  synthesized with and without glucose additive and (b) for  $\text{Na}_2\text{FeM}(\text{SO}_4)_3/\text{C}$  M=Fe, Mn, Ni composites.

Both materials exhibited thermally activated conductivity. The activation energy of the composite sample shows a change at about  $260^\circ\text{C}$ , indicating change of the mechanism of conductivity and a stronger contribution of ionic conductivity at higher temperature range.

The activation energies for carbon free  $\text{Na}_2\text{Fe}_2(\text{SO}_4)_3$  and  $\text{Na}_2\text{Fe}_2(\text{SO}_4)_3/\text{C}$  composite are significantly different. The activation energy of the former was estimated to be 0.56 eV for the whole temperature range, in good agreement both with experimental data (0.50 eV)<sup>31</sup> and theoretical computations 0.55 eV<sup>9</sup>, for the latter the value of apparent activation energy was substantially reduced, to 0.20 eV in the low temperature range and to 0.43 eV in the high temperature range, evidently as a result of electronic conductivity introduced by the carbon film.

For Mn and Ni substituted composite samples,  $\text{Na}_2\text{FeM}(\text{SO}_4)_3/\text{C}$ , a decrease in electrical conductivity was observed (Fig. 8b). At 100 °C total electrical conductivity varied from  $1.56 \cdot 10^{-8} \text{ S cm}^{-1}$  for  $\text{Na}_2\text{FeNi}(\text{SO}_4)_3$ , through  $8.85 \cdot 10^{-8} \text{ S cm}^{-1}$  for  $\text{Na}_2\text{FeMn}(\text{SO}_4)_3$  up to  $4.15 \cdot 10^{-6} \text{ S cm}^{-1}$  for  $\text{Na}_2\text{Fe}_2(\text{SO}_4)_3$ .

As the amount of carbon in all the  $\text{Na}_2\text{FeM}(\text{SO}_4)_3/\text{C}$  composite samples was similar, we believe the differences in the transport properties are not related to the carbon film but to the intrinsic properties of the  $\text{Na}_2\text{FeM}(\text{SO}_4)_3/\text{C}$  composite or to the interface between carbon and the alluaudite.

### 3.6. Sodium storage capacity in low cost and environmental friendly Na-ion batteries

The performance of the electrodes was evaluated in the  $\text{Na} \mid \text{Na}^+ \mid \text{Na}_2\text{FeM}(\text{SO}_4)_3$  half cells through the charging/discharging test and results are depicted in Fig. 9a. According to the *ex-situ* XRD, for  $\text{Na} \mid \text{Na}^+ \mid \text{Na}_2\text{Fe}_2(\text{SO}_4)_3/\text{C}$  cell a monophasic working mechanism was observed (Fig. S7 in Supplementary material). Previous experiment for nonstoichiometric  $\text{Na}_{2.56}\text{Fe}_{1.72}(\text{SO}_4)_3$  phase<sup>32</sup> indicates on the same intercalation/deintercalation mechanism but the volume change, equal  $\Delta V = 5\%$ , is much smaller than for our stoichiometric  $\text{Na}_2\text{Fe}_2(\text{SO}_4)_3$  equivalent  $\Delta V = 19\%$ . Based on that conclusion and low activation energy equal 0.2 eV (Fig. 8), much lower than published before for nonstoichiometric  $\text{Na}_{2.5}\text{Fe}_{1.875}(\text{SO}_4)_3$  one (0.6 eV)<sup>33</sup>, we can suspect that method proposed in here gives the opportunity to obtain the more flexible structure.



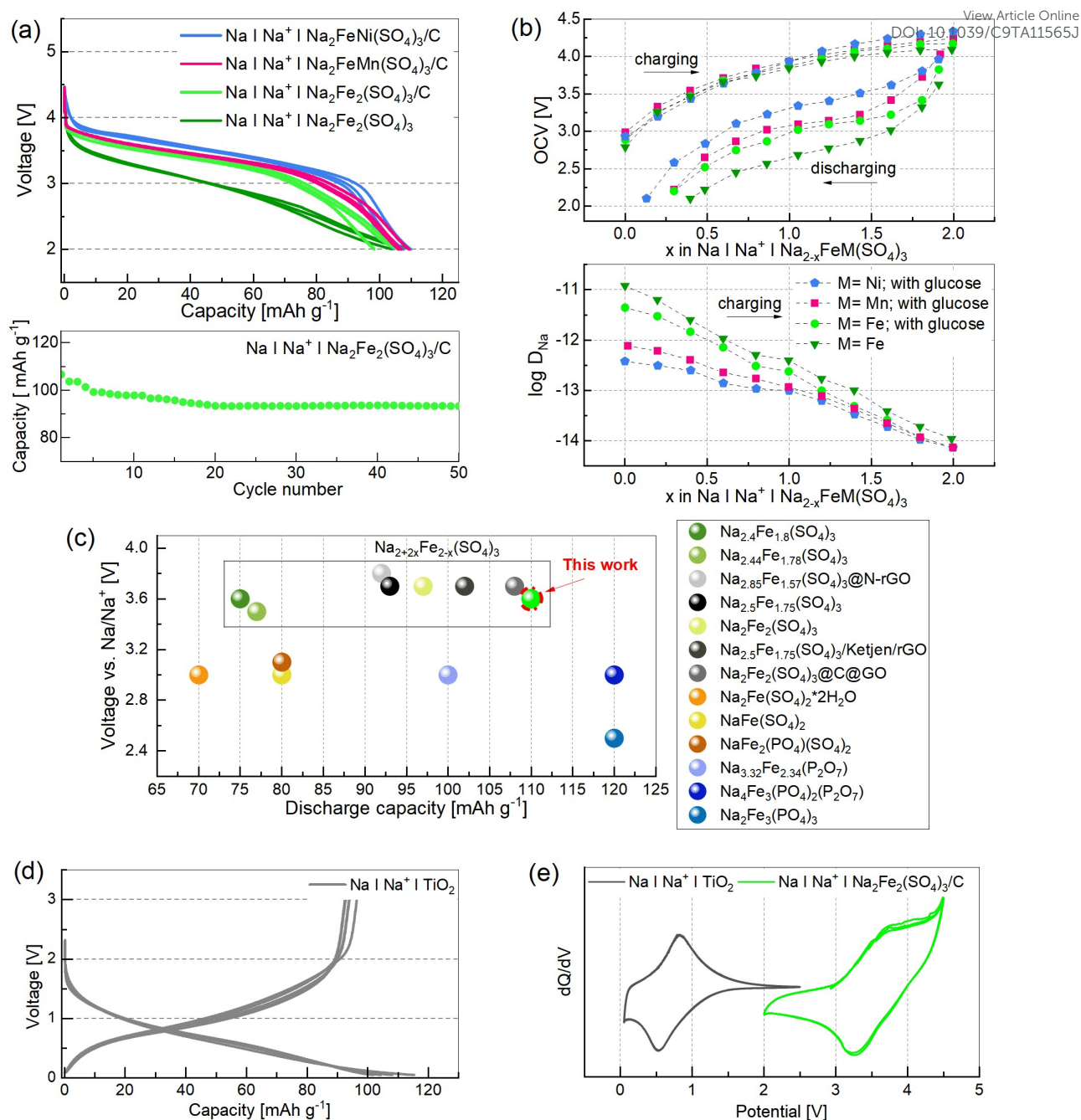


**Fig. 9.** (a) First 3 discharge potential characteristics for  $\text{Na} \mid \text{Na}^+ \mid \text{Na}_2\text{FeM}(\text{SO}_4)_3$  cells and discharge capacity retention on cycling of the  $\text{Na} \mid \text{Na}^+ \mid \text{Na}_2\text{Fe}_2(\text{SO}_4)_3$  cell (current rate  $C/10$ ). (b) Open circuit voltage measured during charging/discharging (current rate  $C/50$ ) and sodium ions diffusion coefficient during the first charging. (c) Comparison of the mid-range working voltage and the discharge capacity of Fe-based polyanions cathode materials, data are taken from <sup>9,16,17,19–21,34–39</sup>. (d) First 3 discharge potential characteristics for  $\text{Na} \mid \text{Na}^+ \mid \text{TiO}_2$ . (e) Comparison of cyclic voltammograms for  $\text{Na} \mid \text{Na}^+ \mid \text{Na}_2\text{Fe}_2(\text{SO}_4)_3$  and  $\text{Na} \mid \text{Na}^+ \mid \text{TiO}_2$  cells.



The potential characteristics for all  $\text{Na}_2\text{FeM}(\text{SO}_4)_3$  electrodes exhibit the same shape for a first few discharge processes (Fig. 9a), which may point out to the fact that the crystal structure of these cathode materials remains unchanged. There is a significant difference in discharge potential profiles between  $\text{Na}_2\text{Fe}_2(\text{SO}_4)_3$  and  $\text{Na}_2\text{FeM}(\text{SO}_4)_3/\text{C}$  obtained with glucose addition during the synthesis. The voltage plateau of  $\text{Na}_2\text{FeM}(\text{SO}_4)_3/\text{C}$  is flatter and longer than that of the bare  $\text{Na}_2\text{Fe}_2(\text{SO}_4)_3$  although the final capacity is similar. It can be understood that carbon coating on the surface of  $\text{Na}_2\text{Fe}_2(\text{SO}_4)_3$  can largely increase electronic conductivity leading to a reduced polarization. Since the discharge rate of C/10 current rate is small enough to effectively deintercalate all accessible Na ions from  $\text{Na}_2\text{Fe}_2(\text{SO}_4)_3$  and  $\text{Na}_2\text{FeM}(\text{SO}_4)_3/\text{C}$  samples. As a result, the negligible difference in the delivered discharge capacity for both materials is observed. At the beginning of the charge/discharge cycles, the discharge capacity for the  $\text{Na}_2\text{Fe}_2(\text{SO}_4)_3/\text{C}$  cathode can reach as high as  $110 \text{ mAh g}^{-1}$ , and the capacity gradually reduced until about the 20<sup>th</sup> cycle, at which capacity decreased to  $100 \text{ mAh g}^{-1}$ . It is noted that after 20 cycles, the capacity remained almost unchanged. Moreover, the SEM images of  $\text{Na}_2\text{Fe}_2(\text{SO}_4)_3/\text{C}$  cathode layers before and after 50 cycles (Fig. S8 in Supplementary material) show that the carbon coating layers on the active powder after long time cycling remains unchanged. The capacities of  $\text{Na}_2\text{FeNi}(\text{SO}_4)_3/\text{C}$  and  $\text{Na}_2\text{FeMn}(\text{SO}_4)_3/\text{C}$  cathodes are slightly higher than  $110 \text{ mAh g}^{-1}$ . For  $\text{Na}_2\text{Fe}_{1-x}\text{M}_x(\text{SO}_4)_3/\text{C}$ , it is interested to note that the potential plateau increases with substitution by M, namely Mn and Ni, respectively. This observation is similar to the behavior observed for  $\text{LiMPO}_4$  and  $\text{LiMSiO}_4$ <sup>40,41</sup>. The working potentials for  $\text{Na}_2\text{FeNi}(\text{SO}_4)_3/\text{C}$ ,  $\text{Na}_2\text{FeMn}(\text{SO}_4)_3/\text{C}$  and  $\text{Na}_2\text{Fe}_2(\text{SO}_4)_3/\text{C}$  are 3.7 V, 3.6 V, and 3.6 V, respectively, whereas that of  $\text{Na}_2\text{Fe}_2(\text{SO}_4)_3$  is only 3.2 V. In this respect, the contributions of Mn and Ni 3d elements to the overall electrochemical activity of the investigated  $\text{Na}_2\text{Fe}_{1-x}\text{M}_x(\text{SO}_4)_3$  samples need to further clarified. Simple calculations of the theoretical discharge capacity in  $\text{Na}_2\text{FeM}(\text{SO}_4)_3$  assuming only  $\text{Fe}^{2+}/\text{Fe}^{3+}$  redox pair would result in specific capacity of ca.  $60 \text{ mAh/g}$ . As the obtained values of specific discharge capacities for  $\text{Na}_2\text{FeMn}(\text{SO}_4)_3$  and  $\text{Na}_2\text{FeNi}(\text{SO}_4)_3$  cells are ca.  $120 \text{ mAh g}^{-1}$ , it is suggested presence of additional electrochemical processes in addition to  $\text{Fe}^{2+}/\text{Fe}^{3+}$  redox pair activity. DFT computations<sup>10</sup> revealed that electrochemical activity of Mn and Ni in  $\text{Na}_2\text{M}_2(\text{SO}_4)_3$  alluaudite during desodiation should be present at potentials ca. 4.06 and 5.05 V vs.  $\text{Na}^+/\text{Na}$ , which at least for Mn is not observed in OCV studies as well as in charge/discharge cycles in used voltage range

(2.0-4.5 V vs. Na<sup>+</sup>/Na<sup>0</sup> in Fig. 9 a and b) . On the other hand the same DFT studies showed that introduction of the Mn and Ni in the 3d sublattice in Na<sub>2</sub>M<sub>2</sub>(SO<sub>4</sub>)<sub>3</sub> results in shift of the p-type orbitals close to the Fermi level in investigated compounds. Though it could be assumed that, p-type oxygen orbitals being close to the Fermi level in Na<sub>2</sub>FeM(SO<sub>4</sub>)<sub>3</sub> effectively take part in electrode reactions via anionic redox reactions often observed for Li rich NMC electrodes. As such we can then speculate, that Mn and Ni elements do not directly take part in electrode reaction, however indirectly are pushing p-type oxygen orbitals close to Fermi level and therefore triggers the anionic redox activity.

To understand the kinetics of electrode reactions in Na | Na<sup>+</sup> | Na<sub>2-x</sub>FeM(SO<sub>4</sub>)<sub>3</sub> cells, electrochemical impedance spectroscopy (EIS) and open circuit voltage (OCV) measurements were performed to estimate the chemical diffusion coefficient (Fig. 9b). The Nyquist plots were collected during the charging process (current C/50) of Na | Na<sup>+</sup> | Na<sub>2</sub>FeM(SO<sub>4</sub>)<sub>3</sub> cells. The low-frequency Warburg impedance related to the diffusion of Na<sup>+</sup> ions in the bulk and the  $\partial E/\partial x$  of open circuit voltage have been used to determine the Na-ion diffusion coefficient <sup>42</sup>. The D<sub>Na</sub> values start from 10<sup>-11</sup> cm<sup>2</sup> s<sup>-1</sup> for Na<sub>2</sub>Fe<sub>2</sub>(SO<sub>4</sub>)<sub>3</sub> sulfates and 10<sup>-12</sup> for materials substituted by Mn and Ni, but in the finish of charging the values of D<sub>Na</sub> came closer to 10<sup>-14</sup> cm<sup>2</sup> s<sup>-1</sup>. The value of D<sub>Na</sub> for our Na<sub>2</sub>Fe<sub>2</sub>(SO<sub>4</sub>)<sub>3</sub>/C is the same range of magnitude as Na<sub>2</sub>Fe<sub>2</sub>(SO<sub>4</sub>)<sub>3</sub>@C@GO <sup>20</sup>.

Fig. 9c compares several recently reported iron-based polyanions cathode materials with our present work. It is clear that Na<sub>2+2x</sub>Fe<sub>2-x</sub>(SO<sub>4</sub>)<sub>3</sub> group delivers the highest voltage vs. Na/Na<sup>+</sup> among all presented cathode materials. Another sulfates compositions (Na<sub>2</sub>Fe(SO<sub>4</sub>)<sub>2</sub>\*2H<sub>2</sub>O <sup>36</sup>, NaFe(SO<sub>4</sub>)<sub>2</sub> <sup>34</sup> and NaFe<sub>2</sub>(PO<sub>4</sub>)(SO<sub>4</sub>)<sub>2</sub> <sup>37</sup> are characterised by capacity between 70 and 80 mAh g<sup>-1</sup>. Whereas Na<sub>3.32</sub>Fe<sub>2.34</sub>(P<sub>2</sub>O<sub>7</sub>) <sup>35</sup>, Na<sub>4</sub>Fe<sub>3</sub>(PO<sub>4</sub>)<sub>2</sub>(P<sub>2</sub>O<sub>7</sub>) <sup>39</sup> and Na<sub>2</sub>Fe<sub>3</sub>(PO<sub>4</sub>)<sub>3</sub> <sup>38</sup> are distinguished by even higher capacity 120 mAh g<sup>-1</sup>, but lower voltage than that of the sulfate group. Within the non-stoichiometric Na<sub>2+2x</sub>Fe<sub>2-x</sub>(SO<sub>4</sub>)<sub>3</sub> the group Na<sub>2.4</sub>Fe<sub>1.8</sub>(SO<sub>4</sub>)<sub>3</sub> <sup>16</sup> and Na<sub>2.44</sub>Fe<sub>1.78</sub>(SO<sub>4</sub>)<sub>3</sub> <sup>17</sup> show the lowest energy density. Na<sub>2.88</sub>Fe<sub>1.57</sub>(SO<sub>4</sub>)<sub>3</sub>@N-rGO <sup>22</sup> exhibits the highest voltage value but also low capacity. Na<sub>2.5</sub>Fe<sub>1.75</sub>(SO<sub>4</sub>)<sub>3</sub> <sup>29</sup>, Na<sub>2</sub>Fe<sub>2</sub>(SO<sub>4</sub>)<sub>3</sub> <sup>9</sup>, Na<sub>2.5</sub>Fe<sub>1.75</sub>(SO<sub>4</sub>)<sub>3</sub>/Ketjen/rGO <sup>19</sup> and Na<sub>2</sub>Fe<sub>2</sub>(SO<sub>4</sub>)<sub>3</sub>@C@G <sup>20</sup> are characterised by the same voltage but significantly different capacity with current rate C/10. It can be seen that among all of Na<sub>2+2x</sub>Fe<sub>2-x</sub>(SO<sub>4</sub>)<sub>3</sub> our material stands out with the highest capacity ever reported. Compared to stoichiometric Na<sub>2</sub>Fe<sub>2</sub>(SO<sub>4</sub>)<sub>3</sub> compounds our one delivers 13% higher capacity than presented in <sup>9</sup> for

$\text{Na}_2\text{Fe}_2(\text{SO}_4)_3$  synthesized using solid-state reaction, but the same energy density (about 400 Wh  $\text{kg}^{-1}$ ) as  $\text{Na}_2\text{Fe}_2(\text{SO}_4)_3@\text{C}@\text{GO}$  synthesized by carbon-coating freeze-drying process<sup>20</sup>.

To fabricate a full cell, we considered to use commercial anatase  $\text{TiO}_2$  nanopowder as the anode since  $\text{TiO}_2$  was reported to deliver very stable intercalation and deintercalation behavior in Na-ion, as well as in Li-ion batteries<sup>43</sup>. Particularly high electrochemical performance in Na-ion batteries was achieved for phosphorylated  $\text{TiO}_2$  nanotube arrays, which reached capacity beyond 250 mAh  $\text{g}^{-1}$ <sup>44,45</sup>. Therefore, we tested the electrochemical performance of commercial  $\text{TiO}_2$ . The potential profiles for the Na-ion half cells with nano- $\text{TiO}_2$  particle distributed on Al-foil for galvanostatic cycles lies in the 0.05– 1.5 V potential range (C/10 rate) as shown in Fig. 9d. Moreover, voltage profiles for  $\text{TiO}_2$  distributed on Cu foil, long term cycling and CV results are presented in Supplementary material in Fig S8. For a cell where a Cu foil was used as the current collector a slightly higher capacity was observed 100-110 mAh  $\text{g}^{-1}$  than for cells with Al foil 95-110 mAh  $\text{g}^{-1}$ . However, after about 20 cycles, cell capacity stabilizes at 85 mAh  $\text{g}^{-1}$ , regardless of the used collector. On the voltammetric curve shown in Fig. S10d, one cathode and one anode peaks are observed, corresponding to flattening on charging and discharging curves.

There is no clear plateau in its deintercalation although there is a clear plateau at about 1.7V vs  $\text{Li}/\text{Li}^+$ <sup>43</sup>. The capacity of  $\text{TiO}_2$  is about 120 mAh  $\text{g}^{-1}$ . Since this work aimed to study the compatibility of  $\text{TiO}_2$  with  $\text{Na}_2\text{FeM}(\text{SO}_4)_3$  cathodes for full cells, and if aluminum foil can be used with  $\text{TiO}_2$ .

As a proof of concept, sodium ion full cells based on  $\text{Na}_2\text{FeM}(\text{SO}_4)_3$ ,  $\text{TiO}_2$  and  $\text{NaPF}_6$  (EC: DEC) electrolyte were finally fabricated. The voltage range for testing was chosen on a base of the CV characteristics of half cells  $\text{Na}_2\text{FeM}(\text{SO}_4)_3/\text{C}$  and  $\text{TiO}_2$  (Fig. 7e). The detailed electrochemical behaviors with respect to the cathode weight are shown in Fig. 8. The mass ratio of the cathode to anode active materials was about 1.2. The capacity of the full cells was about 50% of the capacity of the half cells which is fairly promising, because as opposed to the sodium half cell, the amount of Na ions in the full cell is fixed, and there are no extra Na source for the parasitic processes occurring during charge/discharge cycling, e.g. formation the SEI layers<sup>46</sup>. Usually, to tackle this issue it is necessary to perform an extra presodiation step for the anode material before assembling full cells<sup>47</sup>. Here, this was omitted and turned out to be not necessary, which can be considered as one of the major advantages

of the described material. The working voltage was about 3.0 V for all tested  $\text{TiO}_2 \text{ I Na}^+ \text{ I Na}_2\text{FeM}(\text{SO}_4)_3$  New Article Online  
DOI: 10.1039/C9TA11565J batteries and 2.9 V for the  $\text{TiO}_2 \text{ I Na}^+ \text{ I Na}_2\text{Fe}_2(\text{SO}_4)_3$  one. Full cells reported in this work exhibited energy density about  $200 \text{ Wh kg}^{-1}$  which is comparable to the other full cells based on  $\text{Na}_{2+2x}\text{Fe}_{2-x}(\text{SO}_4)_3$  for example  $\text{Fe}_2\text{O}_3@\text{graphite}/\text{Na}_{2.4}\text{Fe}_{1.8}(\text{SO}_4)_3$  ( $225 \text{ Wh kg}^{-1}$ )<sup>47</sup> and  $\text{CNT}/\text{Na}_2\text{Fe}_2(\text{SO}_4)_3$  ( $215 \text{ Wh kg}^{-1}$ )<sup>48</sup>. This is a highly encouraging value in comparison to other systems based on polyanion compounds such as  $\text{Sn-C}/\text{NaFePO}_4$  ( $150 \text{ Wh kg}^{-1}$ ),  $\text{CoS}@r\text{GO}/\text{Na}_3\text{V}_2(\text{PO}_4)_3$  ( $92 \text{ Wh kg}^{-1}$ ),  $\text{NiO}/\text{Fe}_2\text{O}_3/\text{Na}_3\text{V}_2(\text{PO}_4)_3$  ( $150 \text{ Wh kg}^{-1}$ ),  $\text{PC-Fe}_3\text{O}_4/\text{Na}_2\text{FeP}_2\text{O}_7$  ( $200 \text{ Wh kg}^{-1}$ )<sup>49</sup>.

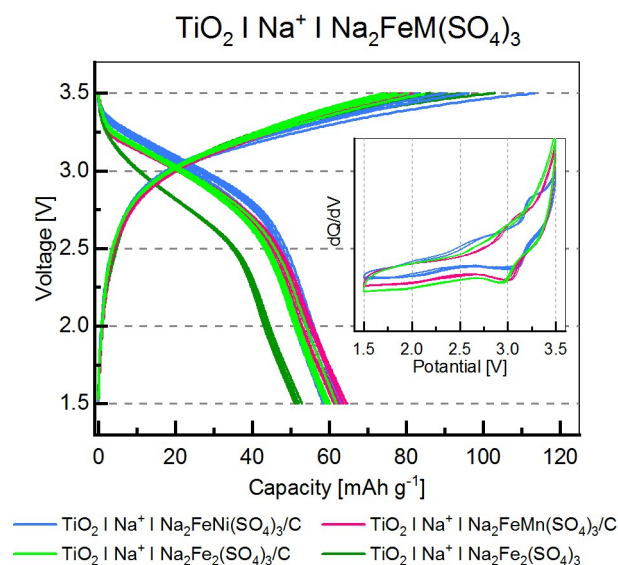


**Fig. 10.** Charge/discharge curves of  $\text{TiO}_2 \text{ I Na}^+ \text{ I Na}_2\text{FeM}(\text{SO}_4)_3/\text{C}$  cells with current  $10 \mu\text{A}$ .

#### 4. Conclusion

The alluaudietes of  $\text{Na}_2\text{FeM}(\text{SO}_4)_3$  ( $\text{M}=\text{Fe}, \text{Mn}, \text{Ni}$ ) were successfully synthesized using a newly developed method. The procedure is simple and relatively quick and based on nontoxic and abundant substrates. Through developing this processing, stoichiometric materials  $\text{Na}_2\text{FeM}(\text{SO}_4)_3$  ( $\text{M}=\text{Fe}, \text{Mn}, \text{Ni}$ ) were achieved. Combination of *in situ* XRD and TG measurements carried out during the synthesis process shed light on a mechanism of formation of the  $\text{Na}_2\text{Fe}_2(\text{SO}_4)_3$  based on phase changing  $\text{P2}_1/\text{c} \rightarrow \text{C2}/\text{c} \rightarrow \text{R-3}$ . SEM technique with EDS, BET and grain size distribution measurements pointed out that this method leads to nanomaterials with a tendency to agglomerate. Sodium ions migration activation energy increased while Fe was substituted, from 0.20 eV  $\text{M}=\text{Fe}$  to 0.58 eV for  $\text{M}=\text{Ni}$ , what is much

lower than presented before and indicates of fast Na ions diffusion with diffusion coefficient around  $10^{-11} \text{ cm}^2 \text{ s}^{-1}$ .  $\text{Na}_2\text{FeM}(\text{SO}_4)_3/\text{C}$  cells represent high voltage systems  $> 3.6 \text{ V}$  with capacity  $110 \text{ mAh g}^{-1}$  ( $1\text{C} = 120 \text{ mAh}$ ) as well as capacity retention above 90% after 50 cycles. Moreover,  $\text{Na}_2\text{FeM}(\text{SO}_4)_3/\text{C}$  cathodes are suitable for full cells  $\text{TiO}_2 \text{ I Na}^+ \text{ I Na}_2\text{FeM}(\text{SO}_4)_3/\text{C}$ , because of extra sodium insertion in alluaudite structure during synthesis which can contribute to the solution of the major problem with deficiency of sodium encountered for many Na-ion and Li-ion full cells.

### Acknowledgments

This work was supported by the National Science Centre - Poland (NCN), grant numbers 2016/21/D/ST5/01658, 2016/23/B/ST8/00199 and 2019/33/B/ST8/00196 and by the National Natural Science Foundation of China, under project number NSFC 51572182. Part of this work was carried out using the infrastructure of the Laboratory of Conversion and Energy Storage Materials in the Centre of Energy, AGH University of Science and Technology.

### References

- 1 M. I. Jamesh and A. S. Prakash, *J. Power Sources*, 2018, **378**, 268–300.
- 2 Q. Ni, Y. Bai, F. Wu and C. Wu, *Adv. Sci.*, 2017, **4**, 1–24.
- 3 S. P. Guo, J. C. Li, Q. T. Xu, Z. Ma and H. G. Xue, *J. Power Sources*, 2017, **361**, 285–299.
- 4 P. Barpanda, *Chem. Mater.*, 2016, **28**, 1006–1011.
- 5 D. Dwibedi and P. Barpanda, *Mater. Res. Soc.*, , DOI:10.1557/adv.2018.
- 6 C. Masquelier and L. Croguennec, *Chem. Rev.*, 2013, **113**, 6552–6591.
- 7 J. Stojanović, T. Dordević and L. Karanović, *J. Alloys Compd.*, 2012, **520**, 180–189.
- 8 A. A. Savina, S. F. Solodovnikov, D. A. Belov, Z. A. Solodovnikova, S. Y. Stefanovich, B. I. Lazoryak and E. G. Khaikina, *New J. Chem.*, 2017, **41**, 5450–5457.
- 9 P. Barpanda, G. Oyama, S. Nishimura, S.-C. Chung and A. Yamada, *Nat. Commun.*, 2014, **5**,

- 1–8.
- 10 R. B. Araujo, S. Chakraborty, P. Barpanda and R. Ahuja, *Phys. Chem. Chem. Phys.*, 2016, **18**, 9658–9665.
- 11 P. Barpanda, D. Dwibedi, R. Gond, A. Dayamani, R. B. Araujo, S. Chakraborty, R. Ahuja and P. Barpanda, *Dalt. Trans.*, **46**, 55–63.
- 12 D. Marinova, V. Kostov, R. Nikolova, R. Kukeva, E. Zhecheva, M. Sendova-Vasileva and R. Stoyanova, *J. Mater. Chem. A*, 2015, **3**, 22287–22299.
- 13 P. Barpanda, *Isr. J. Chem.*, 2015, **55**, 537–557.
- 14 G. Oyama, S. Nishimura, Y. Suzuki, M. Okubo and A. Yamada, *ChemElectroChem*, 2015, **2**, 1019–1023.
- 15 D. Dwibedi, R. B. Araujo, S. Chakraborty, P. P. Shanbogh, N. G. Sundaram, R. Ahuja and P. Barpanda, *J. Mater. Chem. A*, 2015, **3**, 18564–18571.
- 16 D. Dwibedi, C. D. Ling, R. B. Araujo, S. Chakraborty, S. Duraisamy, N. Munichandraiah, R. Ahuja and P. Barpanda, *ACS Appl. Mater. Interfaces*, 2016, **8**, 6982–6991.
- 17 P. B. D. Dwibedi, S. Baskar, *Dalt. Trans.*, 2017, **80**, 337–342.
- 18 H. Wang, Y. Liu, M. Li, H. Huang, H. M. Xu, R. J. Hong and H. Shen, *J. Mater. Chem. A*, 2016, 1166–1169.
- 19 A. Goñi, A. Iturrondobeitia, I. Gil de Muro, L. Lezama and T. Rojo, *J. Power Sources*, 2017, **369**, 95–102.
- 20 M. Chen, D. Cortie, Z. Hu, H. Jin, S. Wang, Q. Gu, W. Hua, E. Wang, W. Lai, L. Chen, S. L. Chou, X. L. Wang and S. X. Dou, *Adv. Energy Mater.*, 2018, **8**, 1–11.
- 21 M. Zhang, H. Qi, H. Qiu, T. Zhang, X. Zhao, H. Yue, G. Chen, C. Wang, Y. Wei and D. Zhang, *J. Alloys Compd.*, 2018, **752**, 267–273.

- 22 W. Wang, X. Liu, Q. Xu, H. Liu, Y. G. Wang, Y. Xia, Y. Cao and X. Ai, *J. Mater. Chem. A*, 2018, **6**, 4354–4364. View Article Online  
DOI: 10.1039/C9TA11565J
- 23 A. Plewa, A. Kulka and J. Molenda, *Patent No. 423612*, Poland, 2017.
- 24 GSAS xrd software, <https://subversion.xray.aps.anl.gov/trac/pyGSAS>.
- 25 Larson A C, *Los Alamos Lab. Rep.*, 1994, **748**, 86–748.
- 26 T. Yamashita and P. Hayes, *Appl. Surf. Sci.*, 2008, **254**, 2441–2449.
- 27 S. Zhou, G. Barim, B. J. Morgan, B. C. Melot and R. L. Brutchey, *Chem. Mater.*, 2016, **28**, 4492–4500.
- 28 A. P. Grosvenor, B. A. Kobe, M. C. Biesinger and N. S. McIntyre, *Surf. Interface Anal.*, 2004, **36**, 1564–1574.
- 29 S. Wei, M. De Boisse, G. Oyama and S. Nishimura, *ChemElectroChem*, 2016, **5**, 209–213.
- 30 <http://abulafia.mt.ic.ac.uk/shannon/ptable.php>.
- 31 J. Lu and A. Yamada, *ChemElectroChem*, 2016, **3**, 902–905.
- 32 G. Oyama, O. Pecher, K. J. Gri, S. Nishimura, R. Pigliapochi, C. P. Grey and A. Yamada, *Chem. Mater.*, 2016, **28**, 5321–5328.
- 33 S. Nishimura, Y. Suzuki, J. Lu, S. Torii, T. Kamiyama and A. Yamada, *Chem. Mater.*, 2016, **28**, 2393–2399.
- 34 P. Singh, K. Shiva, H. Celio and J. B. Goodenough, *Energy Environ. Sci.*, 2015, 3000–3005.
- 35 M. Chen, L. Chen, Z. Hu, Q. Liu, B. Zhang, Y. Hu, Q. Gu, J. Wang, L. Wang, X. Guo and S. Chou, *Adv. Energy Mater.*, 2017, **29**, 1605535.
- 36 P. Barpanda, G. Oyama, C. D. Ling and A. Yamada, *Chem. Mater.*, 2014, **26**, 2013–2015.
- 37 H. Ben Yahia, R. Essehli, R. Amin, K. Boulahya and T. Okumura, *J. Power Sources*, 2018, **382**, 144–151.



- 38 W. Huang, B. Li, F. Saleem, X. Wu and J. Li, *Chem. A Eur. J.*, 2015, **20**, 1–11. View Article Online  
DOI: 10.1039/C9TA11565J
- 39 J. Yeong, H. Kim, Y. Lee, K. Tae, K. Kang and N. Choi, *Electrochem. Commun. J.*, 2014, **44**, 74–77.
- 40 A. Kulka, K. Świerczek, K. Walczak, A. Braun and J. Molenda, *Solid State Ionics*, 2016, **288**, 184–192.
- 41 F. Zhou, M. Cococcioni, K. Kang and G. Ceder, *Electrochem. commun.*, 2004, **6**, 1144–1148.
- 42 P. Xiao, Y. Cai, X. Chen, Z. Sheng and C. Chang, *RSC Adv.*, 2017, **7**, 31558–31566.
- 43 M. O. Guler, O. Cevher, T. Cetinkaya, U. Tocoglu and H. Akbulut, *Energy Convers. Manag.*, 2013, **72**, 111–116.
- 44 J. Ni, S. Fu, C. Wu, J. Maier, Y. Yu and L. Li, *Adv. Mater.*, 2016, **28**, 2259–2265.
- 45 J. Ni, S. Fu, Y. Yuan, L. Ma, Y. Jiang, L. Li and J. Lu, *Adv. Mater.*, 2018, **30**, 1–7.
- 46 W. Ren, Z. Zhu, Q. An and L. Mai, *Small*, 2017, **13**, 1–31.
- 47 X. Ding, X. Huang, J. Jin, H. Ming, L. Wang and J. Ming, *Electrochim. Acta*, 2018, **260**, 882–889.
- 48 J.-M. Tarascon, C. Laberty, C. M. Ghimbeu, C. Vix-Guterl and B. Zhang, *Adv. Energy Mater.*, 2015, **6**, 1501588.
- 49 J. Deng, W. Bin Luo, S. L. Chou, H. K. Liu and S. X. Dou, *Adv. Energy Mater.*, 2018, **8**, 1–17.